nature portfolio

https://doi.org/10.1038/s41563-021-01148-3

Supplementary information

Fabrication and nanophotonic waveguide integration of silicon carbide colour centres with preserved spin-optical coherence

In the format provided by the authors and unedited

Supplementary information for: Nanofabricated and integrated colour centres in silicon carbide with high-coherence spin-optical properties

Charles Babin[1],* Rainer Stöhr[1], Naoya Morioka[1,2], Tobias Linkewitz[1], Timo Steidl[1], Raphael Wörnle[1], Di Liu[1], Erik Hesselmeier[1], Vadim Vorobyov[1], Andrej Denisenko[1], Mario Hentschel[3], Christian Gobert[4], Patrick Berwian[4], Georgy V. Astakhov[5], Wolfgang Knolle[6], Sridhar Majety[7], Pranta Saha[7], Marina Radulaski[7], Nguyen Tien Son[8], Jawad Ul-Hassan[8], Florian Kaiser[1],† and Jörg Wrachtrup[1]

[1] *3rd Institute of Physics, IQST, and Research Center SCoPE, University of Stuttgart, 70569 Stuttgart, Germany*
[2] *Institute for Chemical Research, Kyoto University, Uji, Kyoto, 611-0011, Japan*
[3] *4th Institute of Physics, IQST, and Research Center SCoPE, University of Stuttgart, 70569 Stuttgart, Germany*
[4] *Fraunhofer Institute for Integrated Systems and Device Technology IISB, Schottkystr. 10, 91058 Erlangen, Germany*
[5] *Helmholtz-Zentrum Dresden-Rossendorf, Institute of Ion Beam Physics and Materials Research, 01328 Dresden, Germany*
[6] *Department of Sensoric Surfaces and Functional Interfaces, Leibniz-Institute of Surface Engineering (IOM), 04318 Leipzig, Germany*
[7] *Department of Electrical and Computer Engineering, University of California, Davis, CA 95616, USA*
[8] *Department of Physics, Chemistry and Biology, Linköping University, SE-58183 Linköping, Sweden*

CONTENTS

S1. V_{Si} IMPLANTATION EXPERIMENTS

In this section, we provide additional information on the different implantation techniques used to generate V_{Si} colour centres. In particular, we compare defect generation via implantation of protons, He^+ ions and Si^{2+} ions.

A. Defect generation via helium ion implantation

The key results and implantation parameters have already been discussed in the main text. In this section, we provide additional information on experiments that were carried out to infer the implantation yield and accuracy. To underline reproducibility, we also show the resonant excitation spectra of five additional V2 centres.

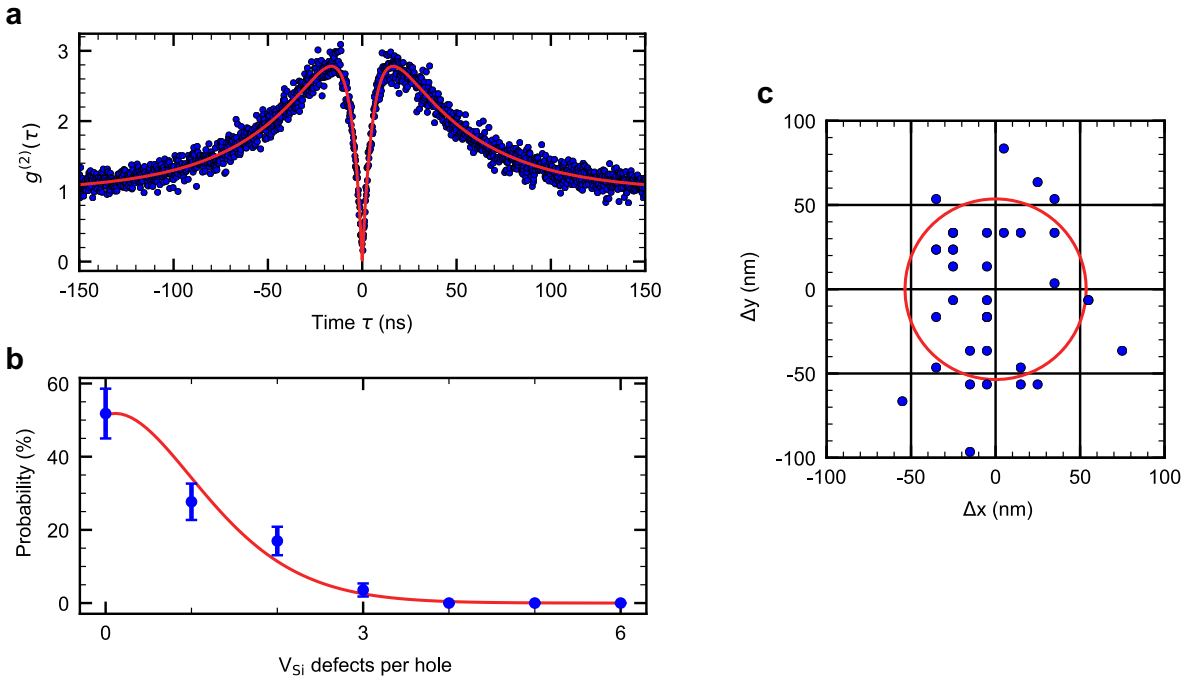

Figure S1. **a** Typical second order correlation measurement of a single V2 centre. Blue dots are data and the red line is a fit taking into account the below-described function for $g^{(2)}(\tau)$. **b** Probability distribution of the number of V2 centres per implantation site. Blue dots are data and error bars correspond to the square root of the number of measurements. The red line is a fit to the data considering a Poissonian distribution. **c** Lateral spatial distribution of the implanted single V2 centres compared to a simulated grid. The red circle represents the 53.6 nm variance of all positions.

1. *Implantation yield*

The implantation yield is defined as the number of V2 centres created per implanted ion. To infer the number of defects per implantation spot, we perform a Hanbury Brown and Twiss interferometry. We record the second-order correlation function ($g^{(2)}$) under off-resonant excitation (785 nm with 2 mW pump power). Note that we are only interested in the yield for generating V2 centres. However, we find that V2 and V1 centres [13] are created at roughly the same rate. To suppress spurious phonon sideband emission of V1 centres during the $g^{(2)}$ measurements, we use a 950 ± 25 nm bandpass filter which rejects most of the V1 centre's emission, and, at the same time, shows a high transmission for in the first phonon sideband of the V2 centre emission (see Figure S6**a**).

A typical measurement is shown in Figure S1**a**. In general, the data can be fitted with the function $g^{(2)}(\tau) = \frac{1}{N}[1-a\cdot e^{-\frac{|\tau|}{\tau_1}}+(1-a)\cdot e^{-\frac{|\tau|}{\tau_2}}]+\frac{N-1}{N}$. Here, τ is the delay time between two detector clicks in the Hanbury Brown and Twiss setup, a is a prefactor, $\tau_{1,2}$ are decay constants, and N is the number of emitters in a spot. In the measurement

shown in Figure S1**a**, we find $g^{(2)}(\tau = 0) \ll 0.5$, which corroborates a single emitter (value extracted from the fit: $N = 1.01 \pm 0.02$). By inquiring 112 spots in the array, we extract the statistical distribution of defect number, shown in Figure S1**b**. The fit to the data is based on a Poissonian function from which we determine the average number of V2 centres created per spot to be 0.66 ± 0.06. Considering the ion implantation dose ($1 \cdot 10^{11}\,\mathrm{cm}^{-2}$) and the mask's hole size (100 nm diameter), we obtain therefore an implantation yield of $8.5 \pm 0.8\%$ for generating V2 centres.

2. *Implantation accuracy*

To estimate the spatial implantation accuracy in lateral coordinates, we use a closed-loop piezo scanner (Mad City Labs Inc. Nano-LPMW, 0.4 nm resolution) and determine the position of 36 single V2 centres within a 12×12 array. Each single-defect position is determined using a two-dimensional Gaussian fit. To infer the principal implantation accuracy, we compare the implantation positions with a simulated grid. We minimize error squares between data and simulation by allowing the simulated grid to account sample rotation and scanner linearity error in both directions. The deviation between the measured data and simulated grid positions is shown in Figure S1**c**. The variance of the defect positions is 53.6 nm (represented by a circle). This value is almost completely determined by the implantation hole size (50 nm diameter), such that the lateral straggle of He^+ ions during implantation is minimal. This is confirmed by SRIM simulations for implanting 6 keV He^+ ions into SiC that predict a lateral projected straggle of 22 nm. The implantation accuracy at this low energy is thus sufficient for creating defects in the centre of photonic crystal cavities.

3. *Implantation depth*

Simulations of helium ion implantation and corresponding vacancy generation have been carried out using the Synopsys Sentaurus Monte Carlo (MC) simulator in order to take the crystalline structure of 4H-SiC into consideration. Sentaurus MC uses the binary collision approximation (BCA). Implantation was simulated at a temperature of $T = 300$ K into the (1 1 -2 0) plane with an implantation energy of 6 keV and a dose of $1 \cdot 10^{11}\,\mathrm{cm}^{-2}$. As we do not have a precise control on the implantation angle in our implanter device, we perform simulations for a variation of tilt angles between 0° and 7°. For the simulation of vacancy generation, threshold displacement energies of 41 eV for Si and 16 eV for C have been chosen for the Frenkel pair defect model while taking into account all secondary recoils from cascades [14]. Figure S2**a** shows the results for implantation at an angle of 0°. Here, we observe a small He^+ ion channelling effect for implantation. However, no channelling is found in the depth profiles of carbon vacancies (V_C) and especially not for V_{Si}. Further simulations at an implantation angle of 7°, shown in Figure S2**b**, shows essentially the shape of the depth profile, however with a $\approx 3\times$ higher defect generation efficiency. Figure S2**c** shows the simulated V_{Si} depth profiles at different implantation angles ranging from 0° to 7°. The general shape of all profiles is the nearly identical, thus confirming that the V_{Si} centres are created in majority at a depth of $30 - 40$ nm.

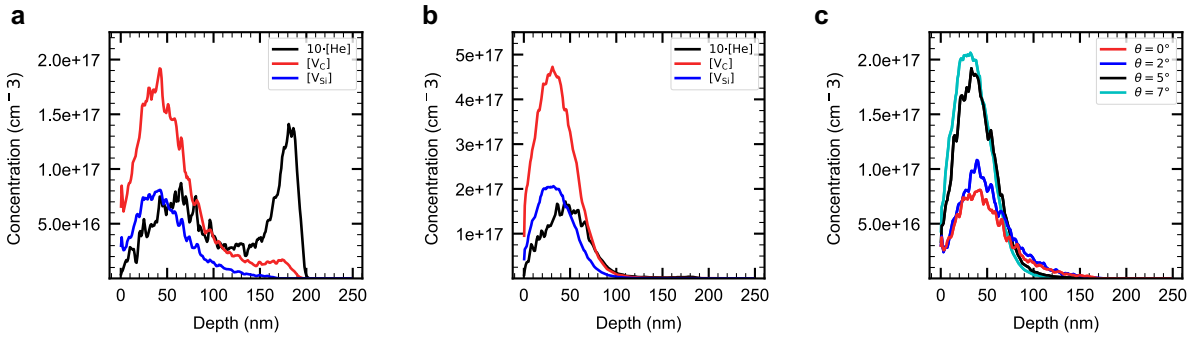

Figure S2. Implantation depths for bombardment with He^+ ions at an energy of 6 keV along the (1 1 -2 0) side of 4H-SiC. In both plots, the black line represents the stopping distance for the He^+ ions, the green line represents the depths at which carbon vacancies are created (V_C) and the blue line shows the V_{Si} depth profiles. **a** Implantation at normal incidence (0°). **b** Implantation at an incidence angle of 7° with respect to the surface normal. Although the peak of the V_{Si} formation density is $\approx 3\times$ higher in **b**, no significant change in the depth profile is observed. **c** V_{Si} depth profiles at different implantation angles ranging from 0° to 7°.

4. *Stability of the resonant absorption lines*

To confirm that implanted V2 centres reproducibly show a good spectral stability, we show here resonant absorption line measurements on another five implanted defects. For each defect, we show repeated laser excitation scans for 20 minutes. The results are shown in Figure S3**a-e**.

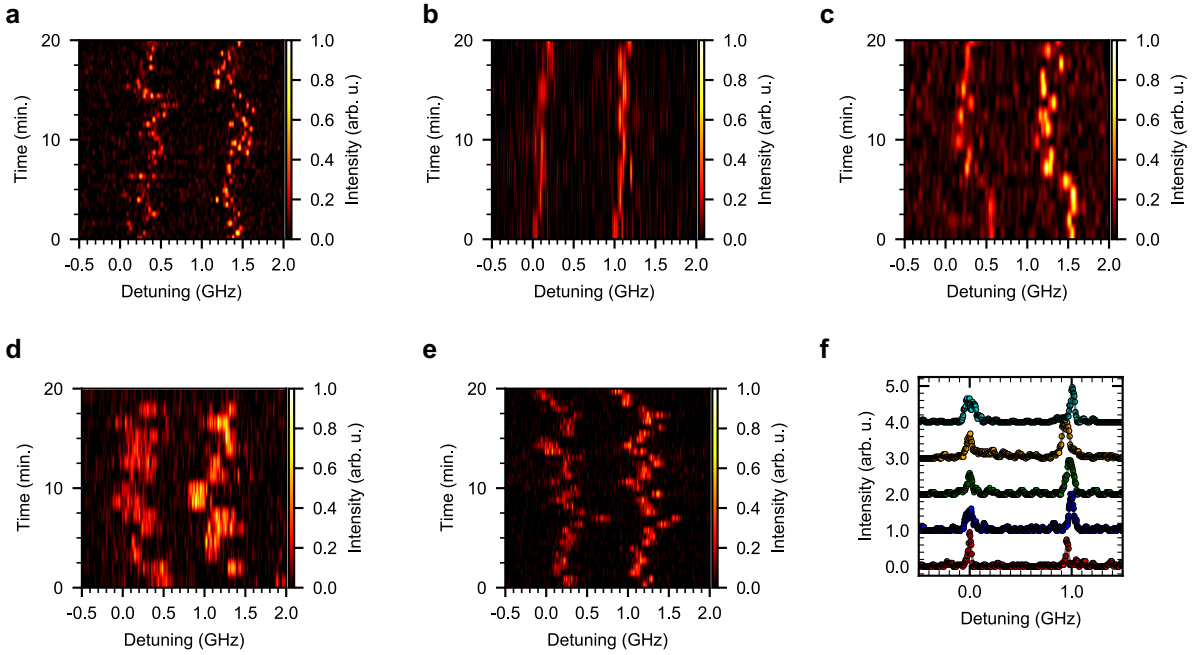

Figure S3. **a-e** Repeated resonant excitation scans during 20 minutes without repump laser for five implanted defects. **f** Single-line resonant excitation scans for five different V2 centres created via He^+ implantation. For better visibility, the A_1 optical transition for all spectra is centreed at zero detuning (the actual spectral distribution of the defects is ± 10 GHz). Each measurement is additionally off-setted by one unit in y-direction. Linewidths are obtained via double-Lorentzian fits to the data. The obtained linewidths for the A_2 (A_1) transitions are (from bottom to top): 25 ± 1 MHz (26 ± 1 MHz), 45 ± 1 MHz (70 ± 2 MHz), 64 ± 2 MHz (52 ± 3 MHz), 79 ± 2 MHz (68 ± 4 MHz); 41 ± 1 MHz (101 ± 3 MHz).

Remarkably, all defects show no signs of ionisation or blinking and single scans result in well-separated spin-selective lines. The very small remaining drift rate can be captured by our laser feedback system (see section S2 E). In Figure S3**f**, we display a single absorption line scans for the five additional defects from which we extract the linewidths of the A_2 and A_1 transitions via double-Lorentzian fit functions.

The average linewidth of the A_2 transition is 46 ± 20 MHz, where the uncertainty is taken from the standard deviation. Our results highlight the reproducibility of our implantation technique to generate high quality colour centres.

B. Proton implantation

We investigate also V2 centre creation via proton implantation. As for the Helium implantation, we use a PMMA mask of 200 nm thickness on which 100 nm diameter holes are patterned using electron-beam lithography. Protons are implanted at an energy of 12 keV at a dose of $5 \cdot 10^{12}\,\mathrm{cm}^{-2}$. The sample is subsequently annealed at 600°C in argon atmosphere for 30 minutes to remove some lattice damage and interstitial defects. A subsequent confocal microscopy image of the implanted defect array is shown in Figure S5**a**. Using the same approach as described in the section S1 A 1 for the Helium implanted defects, we infer the number of defects per spot by measuring the second-order correlation function. A typical $g^{(2)}$ signal is shown in Figure S5**b**. We collect statistical data for 110 implanted spots to infer the average number of V2 centres per spot (see Figure S5**c**). This translates to an implantation yield of $0.83 \pm 0.02\%$ for V2 centres. We also obtain the accuracy of the implantation, using the methods described in section S1 A 2. Similar to the above results, we find a lateral spatial variance of 56 nm, which is almost entirely dominated by the hole size (see Figure S5**d**). This is in accordance with SRIM simulations that predict a lateral projected straggle of 33 nm.

We subsequently measure the resonant absorption spectrum of five generated V2 defects. As shown in Figure S5**a**, single-line scans show spin-conserving transitions lines. From the double-Lorentzian fits, we extract the A_2 (A_1) linewidths, with four fits revealing nearly lifetime limited linewidths. Prolonged repeated measurements for 30 minutes, as seen in Figure S5**b-f**, show no signs of ionisation, but the drift rate is somewhat faster compared to the He^+ ion implanted defects. This is observed despite the fact that proton implanted defects are generated substantially deeper beneath the surface ($\sim$ 110 nm for protons, compared to 40 nm for He^+). Thus, surface charge fluctuations are seemingly not the primary source of spectral drifts. Therefore, we attribute the increased drift rate for proton implanted defects to the increased relative formation of carbon versus silicon vacancies due to the use of lighter ions.

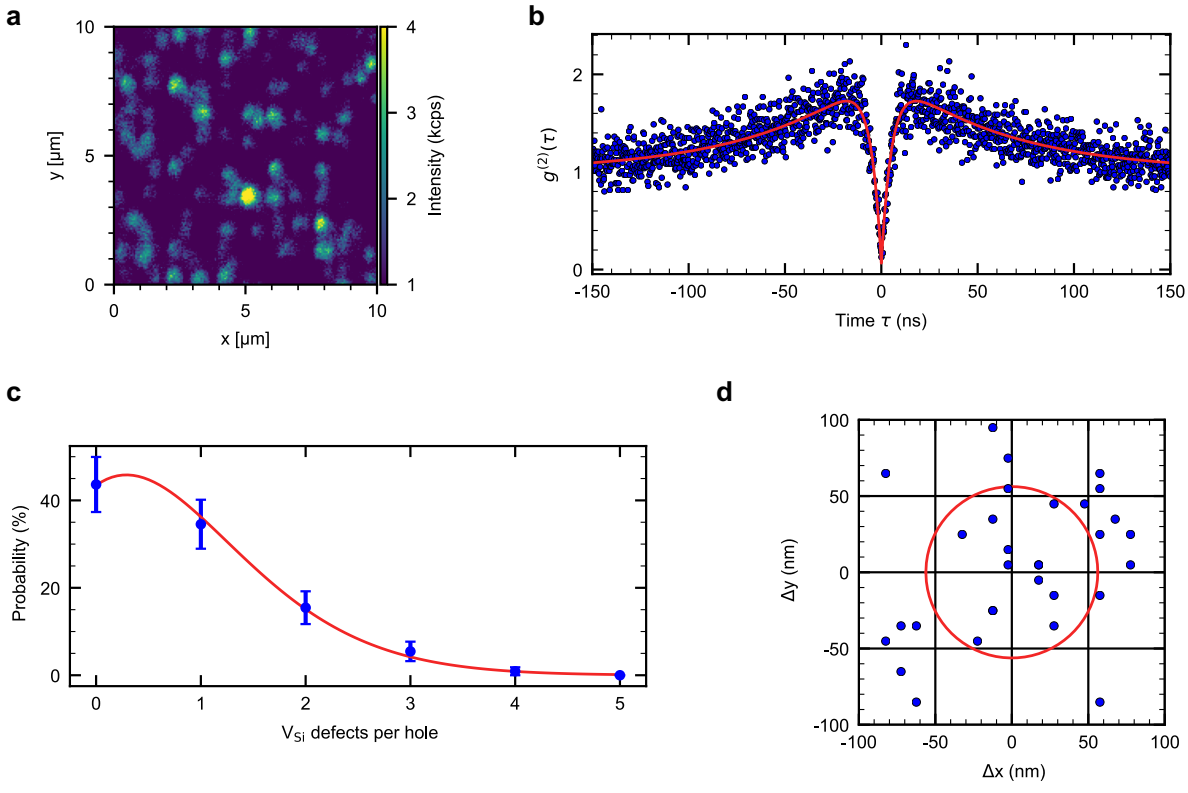

Figure S4. **a** Confocal fluorescence scan of the proton implanted defect centre array **b** Second order correlation function of a single V2 centre. From the fit to the data, we obtain a defect number of $N = 1.07 \pm 0.05$. **c** Probability distribution of the number of created V2 centres per site. The fit to the data is based on a Poissonian distribution. **d** Lateral spatial implantation accuracy compared to the simulated grid. The red circle represents the variance of 56 nm.

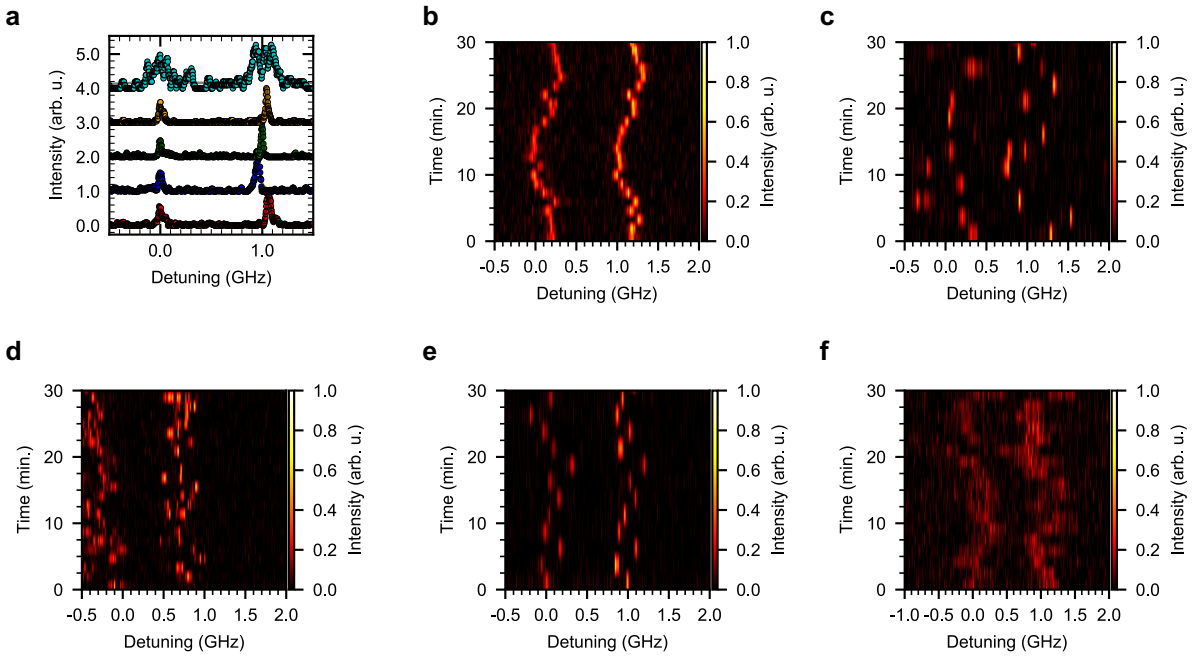

Figure S5. **a** Single-line resonant excitation scans for five different V2 centres created via proton implantation. For better visibility, the A_1 transition for all spectra is centreed at zero detuning. The actual spectral distribution of the defects is ± 10 GHz. The single scan linewidths obtained from the fits are (from bottom to top): 43.9 ± 0.6 MHz (49 ± 2 MHz), 43 ± 1 MHz (39 ± 1 MHz), 20.9 ± 0.4 MHz (30 ± 1 MHz), 25.9 ± 0.5 MHz (37 ± 1 MHz); 226 ± 6 MHz (147 ± 8 MHz) for the A_2 (A_1) transition. **b-f** Repeated resonant excitation scans for 30 minutes without repump laser for five isolated V2 centres. No ionisation is observed. However, the drift rate is somewhat faster compared to the defects created via He^+ implantation.

C. Silicon implantation

We implant Silicon ions (Si^{2+}) using a focussed ion beam device, operating at 35 keV acceleration voltage. The ion flux is varied from the minimal nominal dose of $1 \cdot 10^{-18}$ C per spot to $29 \cdot 10^{-18}$ C per spot, in other words, 3.1 to 91 ions are implanted per spot. After annealing the sample at 600°C for 30 minutes, we investigate the defect arrays at cryogenic temperatures ($T = 10$ K). Unfortunately, even at the lowest implantation dose, we did not observe any single defect.

We record photoluminescence emission spectra of the implanted spots using a Peltier cooled spectrometer (Ocean Insight QE pro, 0.3 nm resolution). A typical measurement is shown in Figure S6**a**. In all implanted spots, we clearly identify the characteristic zero-phonon lines of V1 and V2 centres a 862 nm and 917 nm, respectively. For V2 centres, we usually find ZPL emission linewidths of about 1 nm (see inset of Figure S6**a**), which is in contrast to the 0.3 nm emission linewidths that are obtained for He^+ and proton implanted defects. Thus, without surprise, we were not able to identify resonant absorption lines for those defects.

To further investigate the Si^{2+} implanted defects, we perform additional measurements on the excited state lifetimes of the implanted defects. To this end, we use a 2-ps-pulsed excitation laser that operates at a central wavelength of 780 nm. From the time-dependent phonon sideband fluorescence, we extract the lifetime. The corresponding data is shown in Figure S6**b**. We clearly observe a bi-exponential decay with 1/e-lifetimes of $\tau = 5.63 \pm 0.07$ ns and $\tau = 2.79 \pm 0.09$ ns, respectively. The longer decay constant closely resembles the typical results obtained for off-resonant excitation of V1 and V2 centres [13, 15]. The shorter decay time may indicate that additional non-radiative decay channels have been created due to substantial crystal damage associated with heavy Si^{2+} ion implantation [16, 17]. Our hypothesis is strengthened by the single-decay results that are obtained with Helium and proton implantation (see main text). In future work, it may be interesting to reduce the Si ion flux to single silicon ions, and/or to see whether similar methods could be applied using helium ions.

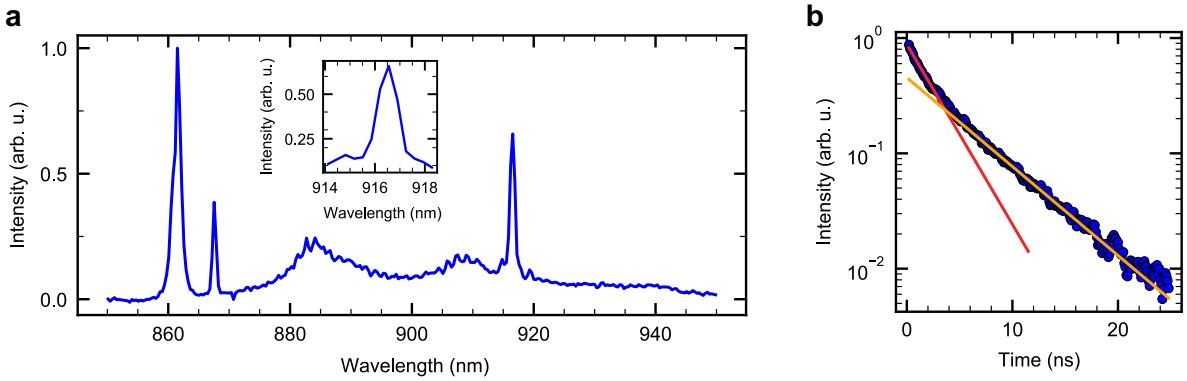

Figure S6. **a** Typical photoluminescence spectrum of an implantation spot using the lowest possible Si^{2+} ion dose of $1 \cdot 10^{-18}$ C. The zero-phonon lines of both V1 and V2 are clearly visible, which clearly show that multiple defects are being generated. The inset shows a zoom-in for the V2 zero-phonon line, which is substantially wider compared to the proton and Helium implanted defects. **b** Pulsed off-resonant excitation lifetime measurement of a single implantation spot. The fit is based on a bi-exponential decay function, yielding 1/e-lifetimes of $\tau = 2.79 \pm 0.09$ ns and $\tau = 5.63 \pm 0.07$ ns, respectively.

S2. WAVEGUIDE INTEGRATED V2 CENTRES

A. Defect density in the waveguide SiC sample

As mentioned in the Methods section, V2 centres have been created in the SiC sample via electron beam irradiation prior to waveguide fabrication. To estimate the expected defect density in the waveguides, we measure the defect density in the bulk material next to the waveguides via standard confocal microscopy. For the scans, we use a continuous-wave excitation laser with an operation wavelength of $\lambda = 785\,\mathrm{nm}$. To estimate the defect density, we need to consider the axial resolution of the microscopy setup. Considering that our microscope objective has a numerical aperture of NA = 0.9, and that the refractive index of 4H-SiC is $n = 2.6$, we obtain an axial resolution of:

$$z_{\mathrm{axial}} = \frac{2\,\lambda}{\mathrm{NA}^2} \approx 1.9\,\mu\mathrm{m}. \tag{S1}$$

We subsequently count 57 defects in a scanning area of $5 \times 15\,\mu\mathrm{m}^2$ in the bulk next to the waveguides, see Figure S7. Assuming that the defects are axially homogeneously distributed over $1.9\,\mu\mathrm{m}$ results in a defect density of $\rho_{\mathrm{V_{Si}}} \approx \frac{57}{142.5\,\mu\mathrm{m}^3} = 0.4\,\mu\mathrm{m}^{-3}$.

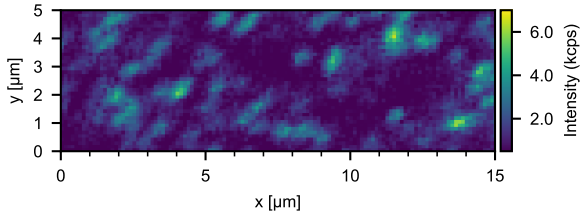

Figure S7. Confocal microscopy scan in the bulk next to the waveguides.

B. Depth scans from waveguides to SiC surfaces

Considering the axial resolution of our microscopy setup, we underetch the waveguides by $\approx 2\,\mu\mathrm{m}$ to ensure that optical excitation is performed on waveguide-integrated defects without spurious signal from defects in the SiC bulk substrate beneath. A typical confocal depth scan is shown in Figure S8**a**. Three waveguides are visible, with fluorescence of defects primarily occurring at the apices. The bulk SiC surface is also visible, including two near-surface defects. Fluorescent spots in waveguides and bulk SiC are well separated, thus confirming that resonant excitation experiments are indeed performed with defects localised in waveguides.

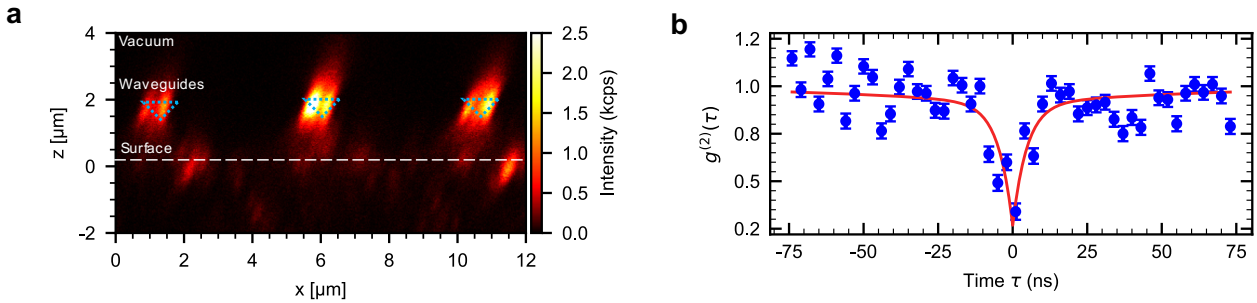

Figure S8. **a** Confocal microscopy depth scan in the waveguide area on the sample. The SiC bulk substrate surface is visible at a depth position $z \approx 0\,\mu\mathrm{m}$. Three waveguides appear at $z \approx 2\,\mu\mathrm{m}$. Defects in the bulk and waveguides appear well-separated, thus permitting selective excitation without spurious parasitic signals. **b** Second order correlation function of a single V2 centre in the waveguide, indicating single emitter behaviour ($g^{(2)}(\tau = 0) < 0.5$).

C. Emission spectra of V_{Si} and non-V2 colour centres in the waveguides

In Figure 2**f** in the main text, we show typical confocal scans along the nanofabricated waveguides at $T = 10\,\mathrm{K}$ with 785 nm continuous wave excitation. Multiple bright spots appear, however, most spots are not identified as V2 centres.

We have attempted to figure out the origin of the remaining fluorescent defects on the waveguides via measuring emission spectra. A typical emission spectrum of these defects and a typical spectrum of a V2 centre are shown in Figure S9. Unfortunately, no distinct features are present in the non-V2 centre spectra, despite the low temperature operation, making it hard for us to attribute the origin of the fluorescence to particular colour centres. At this point, we would like to mention that the identification of colour centre origin/structure is an ongoing field of research for the relatively new SiC platform. Additionally, many studies on unknown defects are performed at room temperature, which complicates a straightforward comparison to our low-temperature experiments. Nevertheless, comparing our spectra to known colour centres (e.g., as nicely summarized in reference [18] and references therein), we can exclude carbon antisite vacancies (CAV), as well as annealing-related defects. Our measured emission spectra show some overlap with unknown defects that have been tentatively attributed to surface oxide [19]. Such an oxide layer may form during the sample nanofabrication and/or acid cleaning. In the end, we would like to mention that the occasional presence of other colour centres on waveguides is not problematic for future experiments that target excitation of defects through the waveguides. Here, it is only important to be able to address individual VSi centres via spin-selective resonant optical excitation. The low powers used for resonant excitation experiments (nW range) are unlikely to induce any sizeable emission of other colour centres, even when performing excitation through the waveguide.

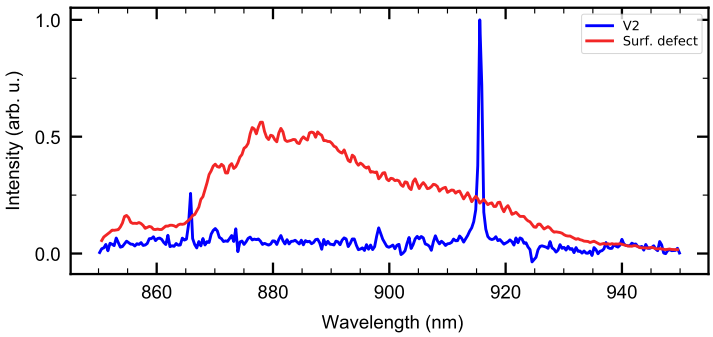

Figure S9. Typical emission spectra of colour centres in waveguides. The red curve represents a typical non-V2 defect, while the blue curve shows the emission spectrum of a V2 centre, which we identify in one out of five waveguides.

D. PLE statistics

To underline the reproducibility of the results presented in the main text, we studied five additional V2 centres in waveguides. To this end, we show repeated resonant excitation scans for five additional defects in different waveguides. Experimental data is shown in Figure S10. All defects exhibit a very slow spectral drift and no ionisation is observed. The single-line scans of those five defects correspond to the upper five data sets in Figure 2**f** in the main text. The extracted single scan linewidths for the A_2 (A_1) transitions of those five defects are 21.4 ± 0.3 MHz (49 ± 2 MHz), 123 ± 7 MHz (115 ± 20 MHz), 17.6 ± 0.3 MHz (32 ± 1 MHz), 78 ± 2 MHz (216 ± 8 MHz), 15.6 ± 0.4 MHz (44 ± 3 MHz), 93 ± 1 MHz (100 ± 5 MHz).

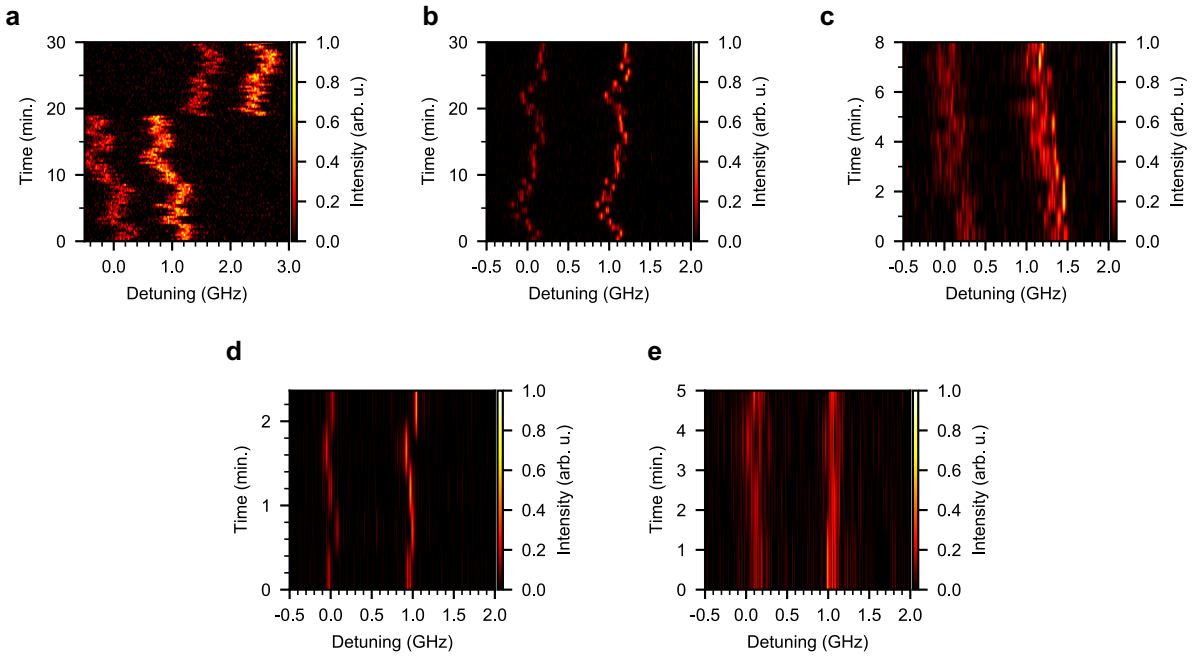

Figure S10. **a-e** Repeated resonant excitation scans for the defects presented in Figure 2**f** of the main text. No ionisation is observed and the remaining drift is assigned to surface charge fluctuations.

E. Laser stabilisation protocol

The resonant absorption lines of our nanofabricated V2 centres still exhibit a very slow drift, e.g., as shown in Figure S10. To perform complex long-term measurements, we thus periodically refocus the resonant excitation laser on the A_2 optical transition. The refocussing period is typically chosen on a time scale of a few to several minutes. The employed protocol is schematically depicted in Figure S11. During all steps in the protocol, we provide a microwave (MW) drive resonant with the ground state transitions $m_S = +1/2 \leftrightarrow m_S = +3/2$ and $m_S = -1/2 \leftrightarrow m_S = -3/2$ to counteract spin pumping by mixing the ground state populations. The laser feedback protocol goes as follows:

(1) We probe whether the absorption lines drifted by applying a resonant excitation on the A_2 optical transition for 500 ms. Provided that more than 300 photons are detected, we consider that no drift occurred, and the main measurement is continued. If less than 300 photons are detected, we proceed with step (2).

(2) We perform up to two resonant excitation scans (PLE), by tuning the resonant excitation laser over a frequency range of 3 GHz. The resulting fluorescence signal is fitted with a double-Lorentzian function. The goodness of the fit is evaluated by several criteria, such as the peak separation that must be within $0.9 - 1.1$ GHz, the peak ratio that must be in the range of $\frac{1}{3}$ to 3, the peak width that must be in the range of 10 to 100 MHz, and the signal-to-background ratio that must exceed 5. If all criteria are met, we fix the laser on the high-frequency transition (A_2 line) and resume the main measurement. The laser scanning window is also reset such that the A_2 transition occurs at 2/3 of the (potential) next scan. If the above criteria are not met, we repeat step (2) one more time. If the criteria are not met after the second attempt, we proceed to step (3).

(3) An off-resonant laser pulse (1 mW, 1 s, 785 nm) is applied to modify/reset the charge environment of the V2 centre. Then, we perform up to two resonant excitation scans with a frequency range of 13 GHz. If the signal can be fitted by a double-Lorentzian function with the same fit criteria as mentioned in (2), we continue with step (2). Note that we do not resume the main measurement directly due to laser drift and hysteresis after extended scan ranges. If step (3) is not successful after two attempts, we proceed with step (4).

(4) Similar to step (3), we step (4) employs the same off-resonant excitation pulse, however followed by a resonant excitation scan covering 20 GHz. This scan range is sufficient to always identify the absorption lines, e.g., we have never observed spectral wandering and distribution beyond this range [20]. Once step (4) is successful, we proceed with step (2).

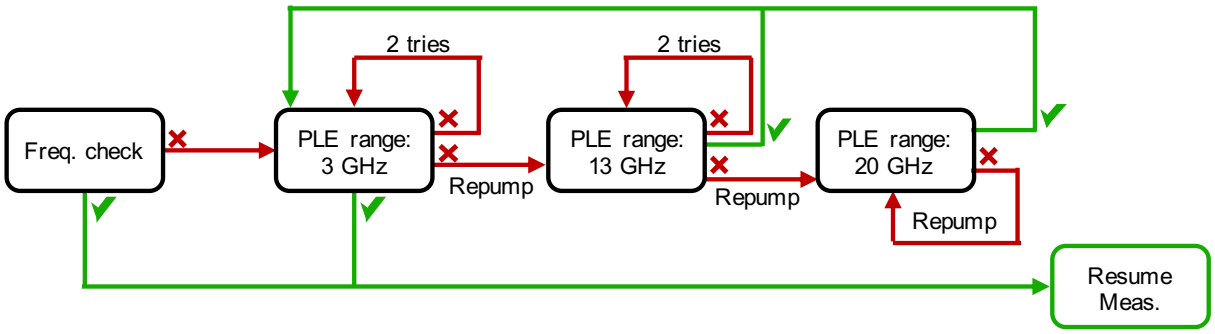

Figure S11. Schematic of the protocol to periodically refocus the resonant laser on the A_2 optical transition of the waveguide-integrated V2 centres. The green (red) arrows correspond to successful (unsuccessful) steps in finding the A_2 transition.

F. Spin properties in bulk material

To infer the spin coherence degradation that V2 centres experience after waveguide fabrication, we compare their spin properties to deep bulk defects that have not been affected by the nanofabrication processes. In the following, we perform Hahn-echo and Ramsey interferometry measurements on a V2 centre that resides in the bulk in a non-etched area on the sample. The results are shown in Figure S12**a**-**b**. From the fit to the data, we obtain a dephasing time of $T^*_{2,\mathrm{bulk}} = 21 \pm 1$ μs and a Hahn echo coherence time of $T_{2,\mathrm{bulk}} = 0.84 \pm 0.03$ ms. Those times are very similar to the ones measured for the waveguide integrated V2 centres, which corroborates that our nanofabrication recipes induce minimal damage.

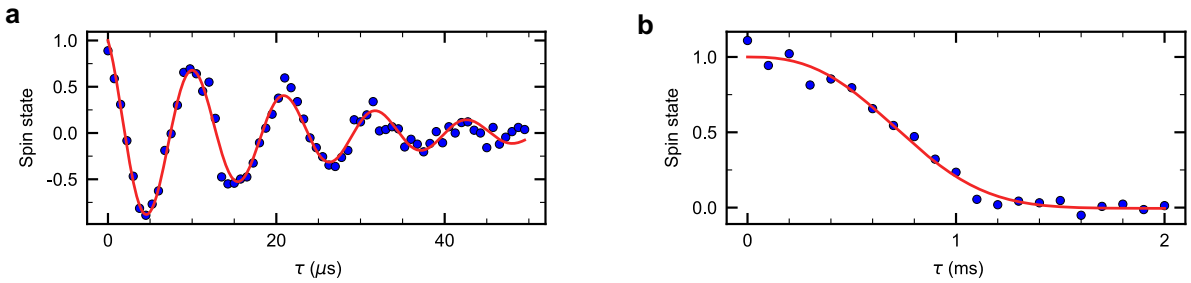

Figure S12. **a** Spin dephasing time for V2 centres in the bulk. From the fit to the data, we obtain $T^*_{2,\mathrm{bulk}} = 21 \pm 1$ μs. **b** Spin coherence time of bulk V2 centres using the Hahn echo sequence. The fit to the data results in a coherence time of $T_{2,\mathrm{bulk}} = 0.85 \pm 0.03$ ms.

G. Optimized waveguide design considering the demonstrated implantation techniques

Our implantation experiments demonstrated that the excellent spin-optical properties of V2 centres are not degraded by He^+ ion implantation and when integrating the defects in nanophotonic waveguides. This promises the development of highly efficient and robust spin-photon interfaces via system integration into waveguides, photonic crystal cavities, and quantum photonic circuits in general. In this section, we discuss ideal waveguide designs based on the demonstrated implantation and nanofabrication techniques.

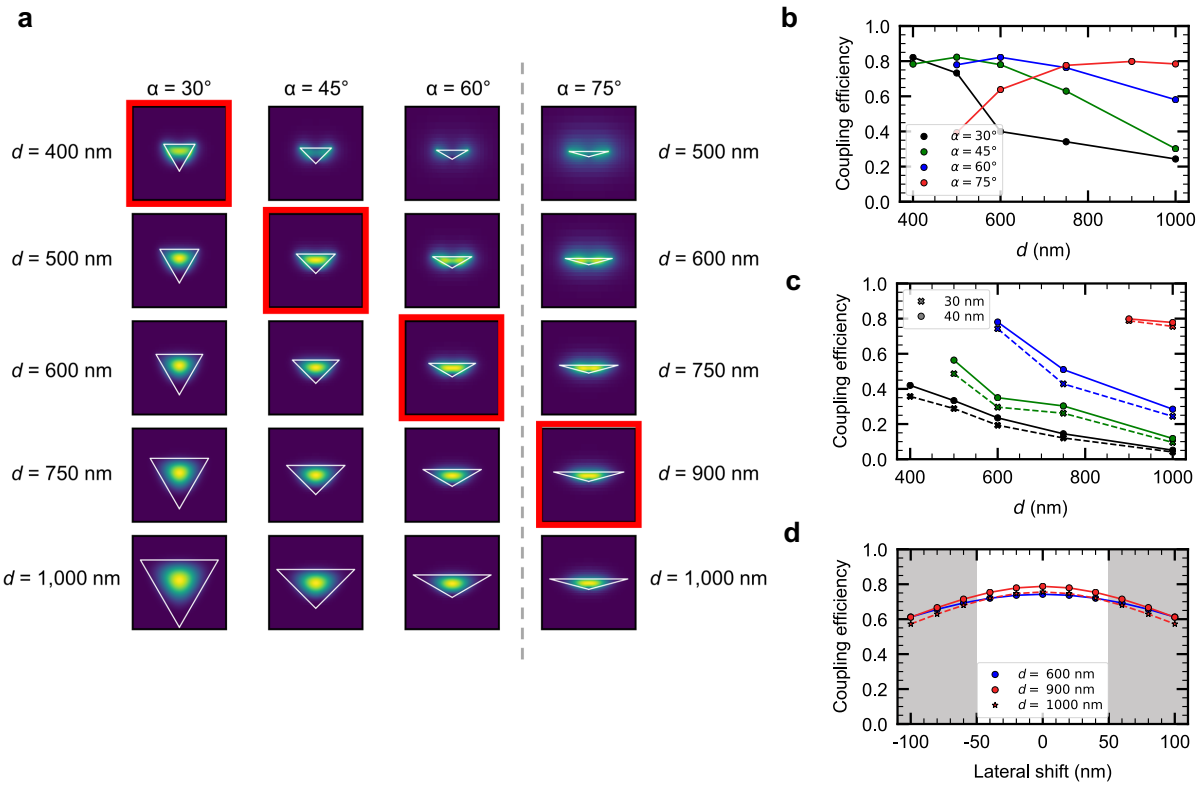

Figure S13. Modelled colour centre emission coupling into a triangular cross section waveguide. **a** TE mode profiles of triangular waveguides with variable etch angle α and width d. Highest waveguide-coupling efficiency is achieved for the devices that are highlighted by a red box. **b** The coupling efficiency of light emitted by a centrally located V2 centre for variable waveguide geometry. **c** The coupling efficiency of light emitted by a V2 centre on the vertical symmetry axis for variable emitter depth and waveguide geometry; the colour legend in **b** applies to the plot. **d** The coupling efficiency of light emitted by a 30 nm deep V2 centre laterally shifted from the central position for variable waveguide geometry; the colour legend in **b** applies to the plot.

In colour centre integration with triangular waveguides, highly efficient single-mode light propagation is a crucial prerequisite for quantum applications. The relationship between device profile and its supported mode wavelength has been modeled recently [21]. Here, we expand on those findings to propose efficient design guidelines for V2 centre emission propagation, robust to the demonstrated implantation uncertainties. In particular, we analyze the coupling efficiency of light emitted by a centrally located horizontal dipole at 917 nm into the transverse electric (TE) modes of a triangular waveguide. We find the existence of the preferential waveguide width d for each studied etch angle α, as presented in Figure S13**a,b**. Interestingly, the mode shape of the optimal device appears more rectangular than circular, and localized within silicon carbide. For the waveguides fabricated in this work ($\alpha = 45°$, $d = 1000$ nm) the coupling efficiency into the fundamental TE mode is approximately 30% (15% in each propagation direction in the waveguide). The efficiency would rise to 82% if those waveguides were minimized to 500 nm width. We note that these coupling efficiencies assume a defect in the centre of the waveguide, i.e., at a depth of 125 nm along the vertical symmetry axis of the devices with $\alpha = 45°$ and $d = 500$ nm. Figure S13**a,b** show additional results for V2 centres positioned in at the centre of different waveguide geometries ($\alpha = 30° - 75°$, $d = 400$ nm $- 1000$ nm). Devices with optimal collection efficiency are highlighted by a red box in Figure S13**a**. Figure S13**b** shows further that waveguides with steeper etching angle α provide high optimal efficiencies over a larger range in d.

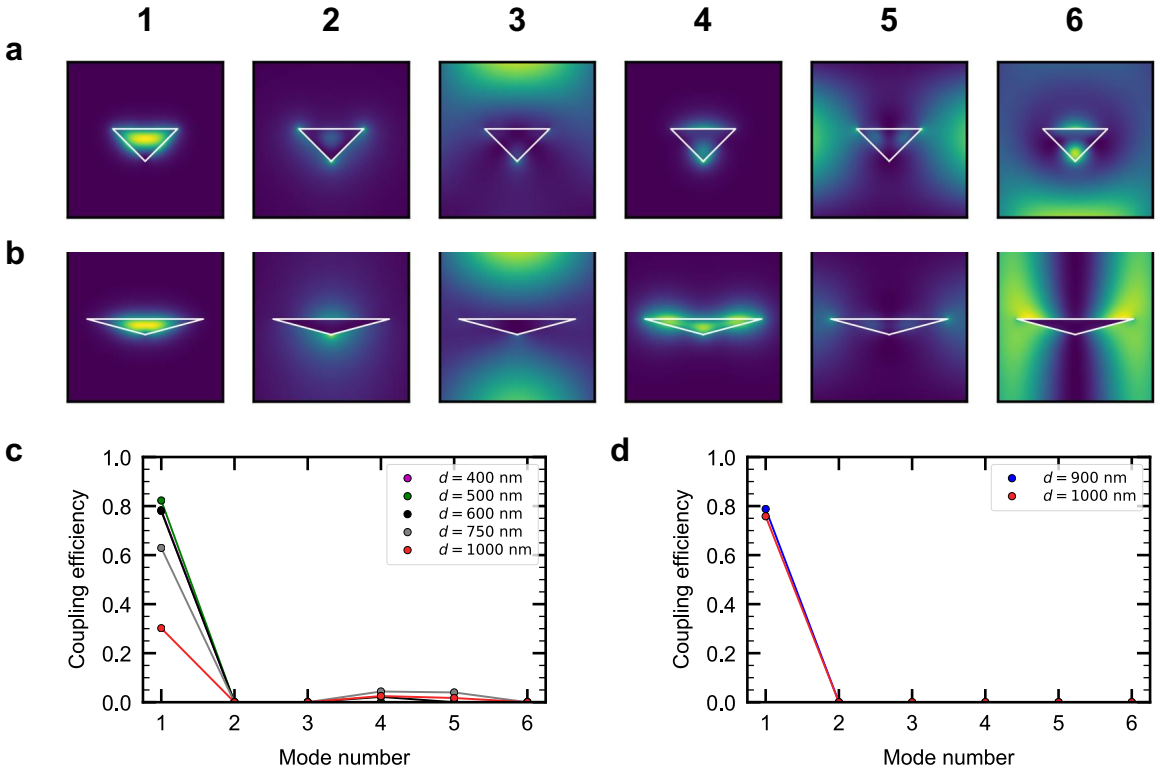

Figure S14. Single mode operation of optimized triangular waveguides. **a** Profiles of the six lowest energy modes supported in a triangular waveguide with etch angle $\alpha = 45°$ and width $d = 500\,\text{nm}$ and **b** etch angle $\alpha = 75°$ and width $d = 900\,\text{nm}$; mode #1 is the fundamental TE polarized mode. **c** The coupling efficiency of light emitted by a centrally located horizontally polarized dipole into each of the modes shown under **a**; the coupling efficiency is evaluated after $10\,\mu\text{m}$ propagation. Single mode operation is observed for waveguide widths of 400 nm and 500 nm. **d** The coupling efficiency of light emitted by a 30 nm deep horizontally polarized emitter to each of the modes shown under b showing single mode operation.

To account for the demonstrated He^+ ions implantation technique that results in a preferred V2 centre creation at $30 - 40\,\text{nm}$ depth, we now provide additional simulation results to identify the optimal geometry. As presented in Figure S13**c**, the coupling efficiency does not change significantly in the investigated depth range ($d = 30 - 40\,\text{nm}$). Devices with higher etch angles result in consistently better coupling efficiencies (up to 80%). Remarkably, the $\alpha = 75°$ devices show very robust coupling efficiencies, especially with regards to the waveguide width $d = 900 - 1000\,\text{nm}$, as shown in Figure S13**c**. We also consider the demonstrated lateral defect creation accuracy which was determined to be $\pm 54\,\text{nm}$ in this work and mainly limited by the implantation mask's hole size (100 nm diameter). As shown in Figure S13**d**, lateral displacement of the emitters does not play a significant role, i.e., fundamental TE mode coupling efficiencies remain within 10% of their peak value. The lost photons couple to the fundamental transverse magnetic (TM) mode and can, in practice, be filtered out by polarisation.

For optimal coupling of light out of the waveguides into single-mode optical fibres, it is important to ensure single TE mode operation. To this end, we simulate the first six TE modes for devices with ($\alpha = 45°$, $d = 500\,\text{nm}$) and ($\alpha = 75°$, $d = 900\,\text{nm}$), respectively. The results are shown in Figure S14**a** and **b**, respectively. The coupling efficiency of from a 30 nm deep emitter to the different modes and varying d is shown in Figure S14**c** and **d**, respectively. We find that both preferred geometries ($\alpha = 45°$, $d = 500\,\text{nm}$) and ($\alpha = 75°$, $d = 900\,\text{nm}$), provide $\approx 80\%$ coupling efficiency into the first TE mode without noticeable excitation of higher-order modes.

Our modelling results show that the demonstrated Faraday cage etching techniques and He^+ ion implantation provide a rich toolset for integrated SiC colour centre photonics. The single TE mode operation of triangular waveguides is highly efficient and robust in multiple degrees of freedom: vertical and lateral emitter displacement, fabrication dimension and surface roughness imperfections. Moreover, these waveguides can be coupled to triangular photonic crystal cavities which are known to provide strong Purcell enhancement utilized to boost the generation of indistinguishable single photons in colour centres [21–23].

S3. PHOTONIC COUPLING IN THE WAVEGUIDE AND OBSERVATION OF LESS V2 CENTRES INSIDE THE WAVEGUIDES

Finite-Difference Time-Domain (FDTD) method is particularly suitable for simulating the expected performance of nanophotonic devices, processes, and materials. This method models the propagation of light by discretizing Maxwell's equations in both time and space coordinates in a leap-frog manner. Owing to high accuracy and broad-frequency response, FDTD method has been widely used as a verification tool for photonic devices over the years. Moreover, FDTD method has been employed to simulate nanocavities in triangular diamond waveguides [23, 24]. Recently, we have used FDTD modeling to analyze color center positioning and Purcell enhancement in triangular SiC waveguides and nanobeam cavities [21]. In this work, as well as in the present manuscript, we have used Lumerical software to perform 3D FDTD electromagnetic simulations, an accurate and widely used tool in academia and industry.

In an attempt to infer the photonic coupling efficiency along the waveguide using our present optical arrangement (collection objective from the top), we performed additional experimental and simulation studies. The basic idea was to infer saturation count rates from V2 centres in the bulk and compare these count rates to emitters in waveguides. Assuming that the total photon emission rate in both cases does not change, and comparing with results from simulations, would then allow to confirm photonic coupling into the waveguide.

Our FDTD model assumes a horizontal dipole emitter in a SiC triangular waveguide (or bulk) studies the light propagation equivalent to the experimental setup. The collection of light into an objective of NA = 0.9 is calculated in a two-step analysis. In the first step, the fraction of light that leaves silicon carbide upwards is evaluated. In the second step, Fourier transform of the electromagnetic field above the structure produces the far-field pattern in k-space, and can be used to calculate the fraction of light that enters the NA = 0.9 objective. The modelling results support the experimental findings and are detailed in Figure S15.

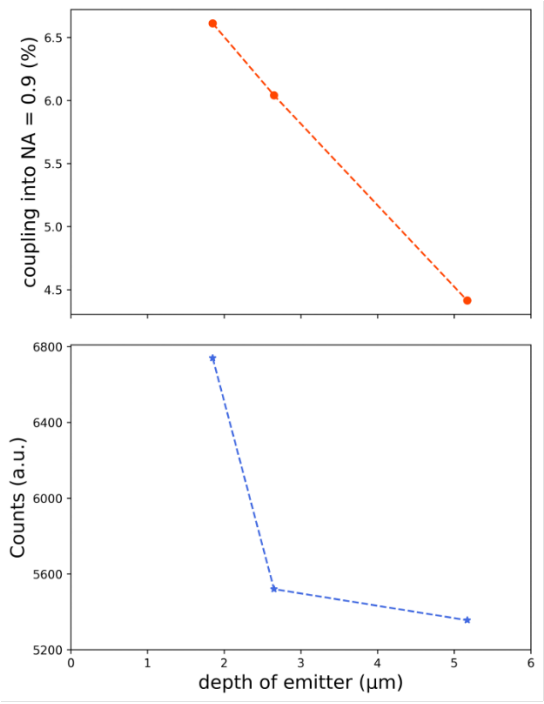

Figure S15. Model of an emitter in bulk. The model of a silicon vacancy in SiC bulk at arbitrary depth (top) shows a decreasing trend in collected photons with the increasing depth of the emitter. Experimental results (below) show a similar trend.

In the next step, we performed simulations on the out-coupling efficiency for defects located in 45° underetched 1000 nm wide waveguides. We found that the collectable photon rate depends very strongly on the exact location of the emitter in the waveguides, see Figure S16.

Considering the large variability of achievable collection efficiency and the limited accuracy towards inferring each defect's precise position inside the waveguide, made it impossible to faithfully measure the saturation count rate, which was therefore not attempted.

These simulations provide also a plausible explanation for the observation of less V2 centres in the waveguides

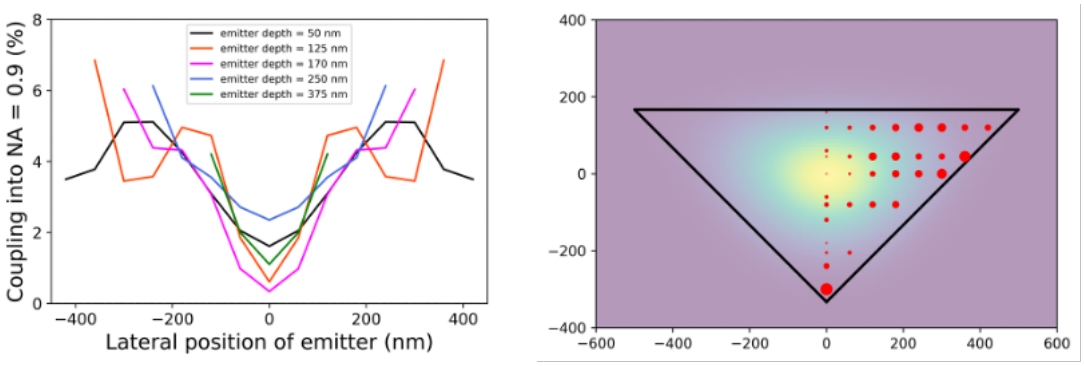

Figure S16. Model of an emitter in a triangular waveguide. The model of a silicon vacancy in a triangular SiC waveguide reveals that collection efficiency into an objective is higher at the edges of the structure than in its center (left). This data supports the experimental findings where emitters are identified at the sides of the structure (see Figure 2f in the Main Text, as well as Figure S8). A plausible explanation is that the emitters that couple to the fundamental mode do not scatter light toward the objective (right). The red dot size is proportional to the light collected by the objective for emitter at that location.

compared to the defect density in the bulk. In this sense, we note that we only identify V2 centres that are bright compared to the waveguide's background fluorescence. This means that we observe only these defects that are placed at ideal positions in the waveguide, notably those that are close to the waveguides' apices, see Figure S16. It is thus very likely that the actual density of negatively charged V2 centres is not modified significantly in the waveguides. As the observed V2 centres show stable optical lines and no ionization, this could indicate that bandbending near the surfaces and edges is not significant.

S4. ELECTRON-NUCLEAR SPIN DYNAMICS

In this section we develop a framework to describe the spin dynamics of a weakly coupled electron-nuclear spin pair during the Hahn echo and CPMG sequences. Further, we provide a methodology to estimate the nuclear spin gate fidelities. We apply the techniques to our hybrid system comprising an electron spin-$\frac{3}{2}$ system coupled to a nuclear spin-$\frac{1}{2}$. However, our framework can be straightforwardly applied to arbitrary electron-nuclear spin systems.

A. Decoupling sequences

1. Hamiltonian

We consider a weakly coupled electron nuclear spin system, such that the secular approximation is valid. Therefore, the Hamiltonian can be expressed as:

$$\hat{\mathcal{H}} = \sum |s_i\rangle \langle s_i| \otimes \omega_i \mathbf{n}_i \cdot \hat{\mathbf{I}} = \sum |s_i\rangle \langle s_i| \otimes \hat{\mathcal{H}}_i. \tag{S2}$$

Here, $|s_i\rangle$ denote the different electron spin levels, and $\hat{\mathbf{I}}$ is the spin matrix representation of the nuclear spin. ω_i and $\mathbf{n}_i$ are the angular frequency and the rotation axis of the nuclear spin when the electron spin is in the state $|s_i\rangle$, respectively. The terms can be expressed as a function of the hyperfine coupling terms as:

$$\omega_i = \sqrt{(s_i A_\parallel - \gamma_n B)^2 + (s_i A_\perp)^2}, \tag{S3}$$

$$\mathbf{n}_i = \frac{1}{\omega_i}(s_i A_\perp, 0, s_i A_\parallel - \gamma_n B). \tag{S4}$$

Here, $A_\parallel$ and $A_\perp$ are the parallel and perpendicular hyperfine coupling terms, respectively. γ_n is the nuclear spin gyromagnetic moment, and B the external magnetic field strength (assumed here to be parallel to the z-axis, which is the electron spin quantisation axis). With this, we now develop the nuclear spin evolution operator with the electron spin state being in the state $|s_i\rangle$ ($\hbar = 1$):

$$\hat{\mathcal{U}}_i(\tau) = \exp\left[-\mathrm{i}(\omega_i \tau)\mathbf{n}_i \cdot \hat{\mathbf{I}}\right]. \tag{S5}$$

In the Bloch sphere representation, this corresponds to a rotation by an angle $\omega_i \tau$ around the axis $\mathbf{n}_i$.

2. Dynamics

The hyperfine coupling can be used to drive the nuclear spin. For a weakly coupled nuclear spin, so-called dynamical decoupling sequences provide a powerful means. By alternating the electron spin between the two states $|s_0\rangle$ or $|s_1\rangle$ (in our case $|s_0\rangle = |m_\mathrm{S} = +1/2\rangle$ and $|s_1\rangle = |m_\mathrm{S} = +3/2\rangle$), the nuclear spin experiences different rotations. We consider the sequence in which the electron spin is initialized into the state $|\psi\rangle_\mathrm{init} = |s_0\rangle$, followed by a $\pi/2$-pulse to obtain the superposition state $(|s_0\rangle + |s_1\rangle)/\sqrt{2}$. Thereafter, we apply the spin manipulation sequence $(\tau - \pi - \tau)^N$, in which, τ represents a waiting time, π a spin-flip pulse, and N is an integer number. If we denote the initial nuclear spin state as $|n\rangle$, then the bipartite system's state at the end of the sequence is:

$$|\Psi\rangle = \frac{1}{\sqrt{2}}\left(|s_0\rangle \otimes (\hat{U}|n\rangle) + |s_1\rangle \otimes (\hat{V}|n\rangle)\right). \tag{S6}$$

Here, $\hat{U}$ ($\hat{V}$) describes the nuclear spin evolution with the electron spin state being $|s_0\rangle$ ($|s_1\rangle$). To simplify the reading, we assume an additional π-pulse at the end of the sequence for even N. This way, we preserve the electron spin state in the case of no nuclear spin being present. After a final $\pi/2$-pulse, the initial electron-spin state $|\psi\rangle_\mathrm{init} = |s_0\rangle$ is preserved with a probability of:

$$P(s_0) = \frac{1 + \cos\left(\frac{\theta_{\hat{V}^\dagger \hat{U}}}{2}\right)}{2}. \tag{S7}$$

Here, $\theta_{\hat{V}^\dagger \hat{U}}$ is the rotation angle of the nuclear spin during the operation $\hat{V}^\dagger \hat{U}$.

B. Hahn echo and modulation

The Hahn echo is a particular case of the decoupling sequence with $N = 1$, in which $\hat{U}$ and $\hat{V}$ are simply:

$$\hat{U} = \hat{\mathcal{U}}_1 \cdot \hat{\mathcal{U}}_0. \tag{S8}$$
$$\hat{V} = \hat{\mathcal{U}}_0 \cdot \hat{\mathcal{U}}_1. \tag{S9}$$

The operators $\hat{\mathcal{U}}_i$ are described in equation (S5). Taking advantage of trigonometric identities

$$\cos(\theta_{1,0}/2) = \cos(\theta_1/2)\cos(\theta_0/2) - \sin(\theta_1/2)\sin(\theta_0/2)\mathbf{n}_1 \cdot \mathbf{n}_0. \tag{S10}$$
$$\sin(\theta_{1,0}/2)\mathbf{n_{1,0}} = \cos(\theta_1/2)\sin(\theta_0/2)\mathbf{n}_0 + \cos(\theta_0/2)\sin(\theta_1/2)\mathbf{n}_1 + \sin(\theta_1/2)\sin(\theta_0/2)\mathbf{n}_1 \times \mathbf{n}_0, \tag{S11}$$

we obtain the well-known equation:

$$P(s_0) = 1 - \frac{k}{4}\left(2 - 2\cos(\omega_0\tau) - 2\cos(\omega_1\tau) + \cos(\omega_+\tau) + \cos(\omega_-\tau)\right). \tag{S12}$$

Here, $\omega_\pm = \omega_0 \pm \omega_1$, and k being the so-called modulation depth parameter:

$$k = \left(\frac{\omega_L A_\perp}{\omega_0\omega_1}\right)^2, \tag{S13}$$

with $\omega_L = \gamma_n B$ being the nuclear spin Larmor frequency.

C. CPMG resonances

For an even number N of π-pulses, the decoupling sequence can be written as: $(\tau\text{-}\pi\text{-}\tau\text{-}\tau\text{-}\pi\text{-}\tau)^{N/2}$, and the operators $\hat{U}$ and $\hat{V}$ as:

$$\hat{U} = \left(\hat{\mathcal{U}}_0 \cdot \hat{\mathcal{U}}_1 \cdot \hat{\mathcal{U}}_1 \cdot \hat{\mathcal{U}}_0\right)^{N/2} = \left(\hat{\mathcal{U}}_{D,1} \cdot \hat{\mathcal{U}}_{D,0}\right)^{N/2}, \tag{S14}$$

$$\hat{V} = \left(\hat{\mathcal{U}}_1 \cdot \hat{\mathcal{U}}_0 \cdot \hat{\mathcal{U}}_0 \cdot \hat{\mathcal{U}}_1\right)^{N/2} = \left(\hat{\mathcal{U}}_{D,0} \cdot \hat{\mathcal{U}}_{D,1}\right)^{N/2}. \tag{S15}$$

Here, $\hat{\mathcal{U}}_{D,i}$ is the composed rotation operator applied to the nuclear spin with the electron spin being in the state $|s_i\rangle$ for a time τ and additionally in the state $|s_{1-i}\rangle$ for another time τ.

To optimize nuclear spin manipulation fidelity, we are now interested in the optimum (resonant) waiting time τ_r at which $\hat{U}$ and $\hat{V}$ are anti-parallel. From equation (S11), we obtain anti-parallel rotation axes if, and only if:

$$\cos(\theta_{D,0}) = \cos(\theta_{D,1}) = 0 \qquad \& \qquad \mathbf{n}_{D,0} \times \mathbf{n}_{D,1} \neq 0. \tag{S16}$$

With equation (S10), we obtain the condition for anti-parallel rotation axes:

$$\tan(\omega_0\tau_r/2)\tan(\omega_1\tau_r/2) = (\mathbf{n}_0 \cdot \mathbf{n}_1)^{-1} \tag{S17}$$

Interestingly, for periodic waiting times $\tau_k = \frac{(2k-1)\pi}{(\omega_0+\omega_1)}$ with $k \in \mathbb{N}^+$, we have $\tan(\omega_0\tau_k/2)\tan(\omega_1\tau_k/2) = 1$. We find further that in the case of negligible perpendicular hyperfine coupling ($|A_\perp| \ll \left|A_\parallel\right|, |\omega_L|$), and with the definition of $\mathbf{n}_i$ in equation (S4), both rotation axes are along the z-axis. The inverse vector product is then $(\mathbf{n}_0 \cdot \mathbf{n}_1)^{-1} \approx 1$. Therefore, we find:

$$\tau_r = \tau_k = \frac{(2k-1)\pi}{\omega_0 + \omega_1}. \tag{S18}$$

This equation represents the zero order approximation, which is exact in the asymptotic cases $B \to \infty$ or $A_\perp = 0$. For more realistic and general cases, the equation needs to be extended with correction terms. In the next section we develop the analytic expression for the first order correction term in $(A_\perp/B)^2$, and we define the criteria for the validity range of the approximation.

1. 1^{st} order correction

We assume $\tau = \tau_k(1+\epsilon_\tau)$, with $\epsilon_\tau \ll 1$. The left side in equation (S17) can be written as a first-order Taylor expansion:

$$\tan(\omega_0\tau/2)\tan(\omega_1\tau/2) = 1 + \epsilon_\tau \cdot \frac{(2k-1)\pi}{\sin(\omega_0\tau_k/2)} + \mathcal{O}(\epsilon_\tau^2). \tag{S19}$$

Then, solving equation (S17) for ϵ_τ results in:

$$\epsilon_\tau = \sin(\omega_0\tau_k/2)\frac{(\mathbf{n}_0 \cdot \mathbf{n}_1)^{-1} - 1}{(2k-1)\pi}. \tag{S20}$$

Considering the vector product in the numerator, one sees from this equation that $\epsilon_\tau \to 0$ for $B \to \infty$. We now develop an expression to define the magnetic field range $B_{\text{crit}} \leq B \leq \infty$ in which the approximation is valid. In other words, given a nuclear spin with coupling terms $A_\parallel$ and $A_\perp$, which is the minimum required magnetic field B_{crit} in which the approximation $\tau_r = \tau_k(1+\epsilon_\tau)$ is valid? To have a negligible contribution from all higher order terms in $\mathcal{O}(\epsilon_\tau^2)$, we want $\epsilon_\tau^2 \ll \epsilon_\tau$, which translates to $(\mathbf{n}_0 \cdot \mathbf{n}_1)^{-1} - 1 \ll \pi$.

2. Validity range for the approximated resonance approximation

From equation (S4), we have:

$$(\mathbf{n}_0 \cdot \mathbf{n}_1)^{-1} = \sqrt{1 + \Big(\frac{A_\perp \cdot \omega_L}{s_1 s_0 \cdot (A_\perp^2 + A_\parallel^2) - (s_0 + s_1) \cdot A_\parallel \cdot \omega_L + \omega_L^2}\Big)^2}. \tag{S21}$$

Therefore, we can define an equivalence as:

$$(\mathbf{n}_0 \cdot \mathbf{n}_1)^{-1} - 1 \leq \epsilon_n \qquad \Leftrightarrow \qquad \Big|\frac{A_\perp \cdot \omega_L}{s_0 s_1 \cdot (A_\perp^2 + A_\parallel^2) - (s_0 + s_1) \cdot A_\parallel \cdot \omega_L + \omega_L^2}\Big| \leq \sqrt{(1+\epsilon_n)^2 - 1}. \tag{S22}$$

Here, $\epsilon_n \ll 1$ is a parameter that is related to the magnitude of the correction term in equation (S19). The last inequality is solved for two solutions:

$$\omega_L + A_- + s_0 s_1 \frac{A_\perp^2 + A_\parallel^2}{\omega_L} \geq 0, \text{ and} \tag{S23}$$

$$\omega_L + A_+ + s_0 s_1 \frac{A_\perp^2 + A_\parallel^2}{\omega_L} \leq 0, \tag{S24}$$

with $A_\pm = (s_0 + s_1)A_\parallel \pm \frac{|A_\perp|}{\sqrt{(1+\epsilon_n)^2 - 1}}$. As required above, we are interested in the solution that covers the case $B \to \infty$, ($B_{\text{crit}} \leq B \leq \infty$). Because $\omega_L = \gamma_n B$, the correct set of solutions depends on the sign of the gyromagnetic ratio γ_n. If γ_n is positive (negative), the inequality to solve is equation (S23) (equation (S24)). To determine the critical magnetic field B_{crit}, we use the following equation:

$$\omega_L^2 + A_{\text{sign}(\gamma_n)} \cdot \omega_L + s_0 s_1 (A_\perp^2 + A_\parallel^2) = 0, \tag{S25}$$

in which $\text{sign}(\gamma_n) = \gamma_n / |\gamma_n|$. Finally we have:

$$(\mathbf{n}_0 \cdot \mathbf{n}_1)^{-1} - 1 \leq \epsilon_n \qquad \Leftrightarrow \qquad B \geq B_{\text{crit}} = \frac{A_{\text{sign}(\gamma_n)} + \text{sign}(\gamma_n)\sqrt{A_{\text{sign}(\gamma_n)}^2 - 4 s_0 s_1 (A_\perp^2 + A_\parallel^2)}}{2\gamma_n}. \tag{S26}$$

Here, we have:

$$A_{\text{sign}(\gamma_n)} = (s_0 + s_1)A_\parallel + \text{sign}(\gamma_n)\frac{|A_\perp|}{\sqrt{(1+\epsilon_n)^2 - 1}}. \tag{S27}$$

We now limit the first-order correction to 10% ($\epsilon_\tau \leq 0.1$) to keep higher order terms at a negligible level. This means that $\epsilon_n = 0.1 \cdot \pi$. With this, we can express the denominator in equation (S27) as $1/\sqrt{(1+\epsilon_n)^2 - 1} \approx 1.17$.

We thus obtain the following theorem for the first-order approximation of the CPMG resonance times τ_r:

Theorem. *For given nuclear spin hyperfine coupling terms $A_\parallel$ and $A_\perp$, and in an external magnetic field along the z-axis with strength B, the CPMG resonances occur at:*

$$\tau_{\text{approx}}^{(k)} = \frac{(2k-1)\pi}{\omega_0 + \omega_1}\Big(1 + \sin\Big(\frac{(2k-1)\pi\omega_0}{2(\omega_0 + \omega_1)}\Big)\frac{(\mathbf{n}_0 \cdot \mathbf{n}_1)^{-1} - 1}{(2k-1)\pi}\Big), \tag{S28}$$

with $k \in \mathbb{N}^+$. This equation is valid as long as $B \geq B_{\text{crit}}$, with:

$$B_{\text{crit}} = \frac{A_{sign(\gamma_n)} + \text{sign}(\gamma_n)\sqrt{A_{\text{sign}(\gamma_n)}^2 - 4 s_0 s_1 (A_\perp^2 + A_\parallel^2)}}{2\gamma_n}, \tag{S29}$$

$$A_{\text{sign}(\gamma_n)} = (s_0 + s_1)A_\parallel + 1.17 \cdot \text{sign}(\gamma_n)|A_\perp|. \tag{S30}$$

3. Application to a particular nuclear spin configuration

We now apply the theorem to the nuclear spin configuration identified in this work, i.e., ($A_\parallel = -23.6\,\mathrm{kHz}$, $A_\perp = 12.2\,\mathrm{kHz}$, $\gamma_n = -84.65\,\mathrm{kHz/G}$). For these parameters, we obtain a critical magnetic field strength of $B_{\mathrm{crit}} = 60.5\,\mathrm{G}$ with an ϵ_τ of the first resonance of $0.083 < 0.1$.

Comparing the approximated value $\tau^{(1)}_{\mathrm{approx}}$ to the numerically solved equation (S17), we find that the relative error is very small, $(\tau_r - \tau^{(1)}_{\mathrm{approx}})/\tau_r = 0.003$. This stands as a clear confirmation for the quality and validity of our first-order approximation and the criteria used to determine the minimum required magnetic field B_{crit}.

Further considering the magnetic field used for the experiment in this work ($B = 81\,\mathrm{G}$), we find that the first-order approximation describes the CPMG resonance time within an error of 0.0026.

Figure S17 shows the error of the approximation $((\tau_r - \tau^{(1)}_{\mathrm{approx}})/\tau_r)$ for varying magnetic field strengths. The horizontal line represents the maximum acceptable error threshold of 0.003 that is obtained with the constraint $\epsilon_\tau \leq 0.1$. The vertical line represents the critical magnetic field strength (B_{crit}). Importantly, the error is below the threshold for any magnetic field exceeding B_{crit}, thus validating our theorem.

This shows that our analytic expression for determining the resonance times in decoupling sequences can be applied even in low magnetic field conditions in which $|\omega_L| \sim |A_\perp|$.

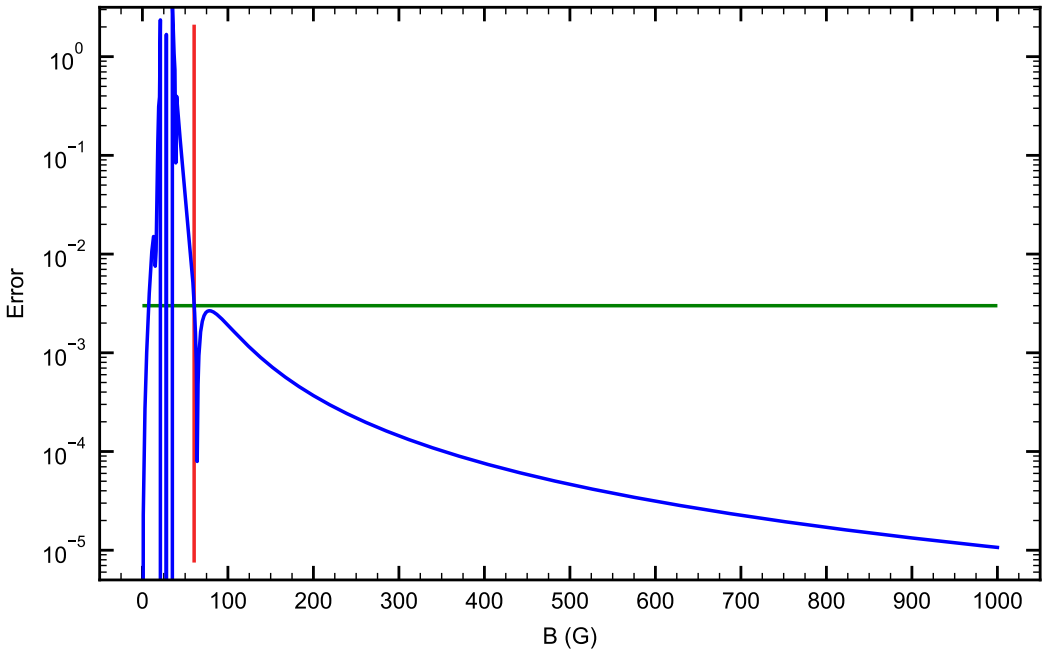

Figure S17. Relative error between the approximated resonance time τ_{approx} and the numerical solution of equation (S17). The red line represents the critical magnetic field from which on the error is always below the defined threshold value (represented by the green line).

D. Obtaining the hyperfine coupling terms

In Figure 2**e** in the main text, we show the Hahn echo signal at a magnetic field strength of $B = 36\,\mathrm{G}$. We use equation (S12) to fit the signal considering coupling between a single V2 centre with a single nuclear spin. By minimizing the error squares between data and fit, we identify that the nuclear spin must be a ^{29}Si nucleus, and we obtain initial hyperfine coupling parameters. However, Hahn echo sequences show a limited precision, such that we perform additional measurements. In particular we perform a 8-pulse CPMG sequence at elevated magnetic field ($B = 81\,\mathrm{G}$), see Figure S18. To simulate the signal, we use the probability given by the equation (S7) in the presence of a single nuclear spin. With the hyperfine coupling parameters extracted from the Hahn echo, we simulated the expected 8-pulse CPMG signal. Although the simulated signal shows a good overlap with the data, we find additional dips at $\tau = 3.7\,\mu\mathrm{s}$, $11.1\,\mu\mathrm{s}$ and $18.5\,\mu\mathrm{s}$, which cannot be explained by the presence of a single nuclear spin. We thus attempt to fit the additional dips with a second nuclear spin and obtain a very good qualitative overlap. Subsequently, all four hyperfine coupling terms are fine-tuned to minimize the error squares between the simulation and the experimental data. In the case of several nuclear spin, the probabilities given by the equation (S7) for each nuclear spin are simply multiply as we neglect any nuclear-nuclear interactions. This allows us to precisely determine that there are two ^{29}Si nuclei with hyperfine coupling terms $A_{\parallel,1} = 2\pi \cdot (-23.5)\,\mathrm{kHz}$, $A_{\perp,1} = 2\pi \cdot 12.0\,\mathrm{kHz}$, $A_{\parallel,2} = 2\pi \cdot 0.2\,\mathrm{kHz}$ and $A_{\perp,2} = 2\pi \cdot 8.5\,\mathrm{kHz}$. To verify our assumption, we simulate, the signal obtained for a varying number of refocusing pulses with $\tau = 5.38\mu\mathrm{s}$. As seen in Figure 2**f**, the oscillations are perfectly described by our model. As the overlap between data and simulations shows now essentially no residuals, we consider that coupling to additional nuclear spins is very weak compared to the electron spin coherence time, and thus negligible. The system is therefore fully described by one electron and two nuclear spins.

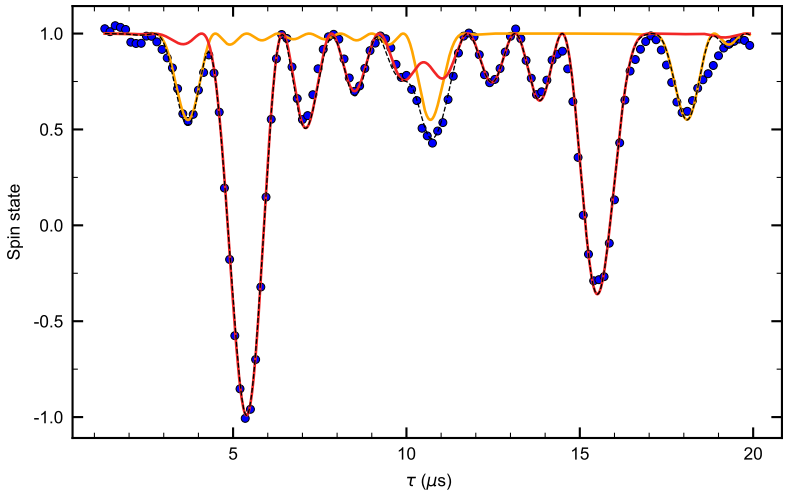

Figure S18. Spin signal for the 8-pulse CPMG sequence at $B = 81\,\mathrm{G}$ (blue dots) and the corresponding contribution of each nuclear spins (red and orange lines). The fit to the data (black dashed line) is based on the product of both contributions.

E. Gate fidelity

In this section, we simulate the evolution of the nuclear spin for decoupling sequences with $\tau = \tau_r$ and varying number of pulses N. From here, we determine the nuclear spin rotation fidelities with respect to relevant quantum gates, such as Hadamard, NOT and I. We use equation S7 and express the evolution operator $\hat{\mathcal{U}}_i(\tau)$ as:

$$\hat{\mathcal{U}}_i(\tau) = \cos\Big(\frac{\omega_i \tau}{2}\Big)\hat{\mathbb{1}} - \mathrm{i}\cdot\sin\Big(\frac{\omega_i \tau}{2}\Big)\mathbf{n}_i\cdot\hat{\mathbf{I}}. \tag{S31}$$

The nuclear spin evolution is simulated with the hyperfine parameters obtained from the fit to the 8-pulse CPMG measurements ($A_\parallel = -23.5\,\mathrm{kHz}$ and $A_\perp = 12.0\,\mathrm{kHz}$ for the first nuclear spin). For $N = 4$, we find that the rotation axes and rotation angles for the operators $\hat{U}$ and $\hat{V}$ are:

$$\mathbf{n}_{\hat{U}} \approx \sqrt{0.943}\cdot\mathbf{e_x} + \sqrt{0.057}\cdot\mathbf{e_z}, \tag{S32}$$

$$\mathbf{n}_{\hat{V}} \approx \sqrt{0.941}\cdot\mathbf{e_x} - \sqrt{0.059}\cdot\mathbf{e_z}, \tag{S33}$$

$$\theta_{\hat{U}} = \theta_{\hat{V}} \approx 0.49\cdot\pi. \tag{S34}$$

We make the following observations:

- The rotation axes are essentially perfectly anti-parallel: $\mathbf{n}_{\hat{U}}\cdot\mathbf{n}_{\hat{V}} = -0.999994$.
- The rotation angles are the same.
- The axis of rotation are (almost entirely) oriented along the $\mathbf{e_x}$ axis.

From the simulation, we now infer the gate fidelities for $N = 4$, 8, 16. To do so, we initialize the bipartite system in one of the four spin-eigenstates, and simulate the spin state $|\Psi_f\rangle$ at the end of the sequence. We then calculate the overlap with the target spin-state as $\mathcal{F} = |\langle\Psi_{\mathrm{target}}|\Psi_f\rangle|^2$. For particular quantum gates, we obtain the following fidelities:

- For $N = 4$, the fidelity for the creation of the Bell state $\left|\Phi_{\mathrm{i}}^{\pm}\right\rangle$ and $\left|\Psi_{\mathrm{i}}^{\pm}\right\rangle$ is $\mathcal{F} = 97\%$.
- For $N = 8$, the fidelity for performing the X-gate on the nuclear spin is $\mathcal{F} = 94\%$.
- For $N = 16$, the fidelity for performing the identity-gate on the bi-partite system is $\mathcal{F} = 98\%$.

We mention that the fidelities could be further improved using an increased external magnetic field. This would further suppress spurious rotation around the $\mathbf{e_x}$ axis. In addition, the nuclear spin rotation angle per CPMG refocussing pulse would decrease, which would allow to precisely tune the number of pulses to implement particular gates. Obviously, the price to pay would be an increased number of refocussing pulses, as well as increased total gate duration times.

* c.babin@pi3.uni-stuttgart.de
† f.kaiser@pi3.uni-stuttgart.de

[1] R. Nagy, M. Widmann, M. Niethammer, D. B. R. Dasari, I. Gerhardt, Ö. O. Soykal, M. Radulaski, T. Ohshima, J. Vučković, N. T. Son, I. G. Ivanov, S. E. Economou, C. Bonato, S.-Y. Lee, and J. Wrachtrup, "Quantum properties of dichroic silicon vacancies in silicon carbide," *Physical Review Applied*, vol. 9, p. 034022, 2018.

[2] W. Li, L. Wang, L. Bian, F. Dong, M. Song, J. Shao, S. Jiang, and H. Guo, "Threshold displacement energies and displacement cascades in 4h-sic: Molecular dynamic simulations," *AIP Advances*, vol. 9, no. 5, p. 055007, 2019.

[3] F. Fuchs, B. Stender, M. Trupke, D. Simin, J. Pflaum, V. Dyakonov, and G. V. Astakhov, "Engineering near-infrared single-photon emitters with optically active spins in ultrapure silicon carbide," *Nature Communications*, vol. 6, no. 1, p. 7578, 2015.

[4] J. R. Weber, W. F. Koehl, J. B. Varley, A. Janotti, B. B. Buckley, C. G. Van de Walle, and D. D. Awschalom, "Quantum computing with defects," *Proceedings of the National Academy of Sciences*, vol. 107, pp. 8513–8518, 2010.

[5] D. McCloskey, D. Fox, N. O'Hara, V. Usov, D. Scanlan, N. McEvoy, G. S. Duesberg, G. L. W. Cross, H. Z. Zhang, and J. F. Donegan, "Helium ion microscope generated nitrogen-vacancy centres in type ib diamond," *Applied Physics Letters*, vol. 104, p. 031109, 2014.

[6] S. Castelletto and A. Boretti, "Silicon carbide color centers for quantum applications," *Journal of Physics: Photonics*, vol. 2, p. 022001, mar 2020.

[7] M. Widmann, M. Niethammer, T. Makino, T. Rendler, S. Lasse, T. Ohshima, J. Ul Hassan, N. Tien Son, S.-Y. Lee, and J. Wrachtrup, "Bright single photon sources in lateral silicon carbide light emitting diodes," *Applied Physics Letters*, vol. 112, no. 23, p. 231103, 2018.

[8] R. Nagy, D. B. R. Dasari, C. Babin, D. Liu, V. Vorobyov, M. Niethammer, M. Widmann, T. Linkewitz, I. Gediz, R. Stöhr, H. B. Weber, T. Ohshima, M. Ghezellou, N. T. Son, J. Ul-Hassan, F. Kaiser, and J. Wrachtrup, "Narrow inhomogeneous distribution of spin-active emitters in silicon carbide," *Applied Physics Letters*, vol. 118, p. 144003, 2021.

[9] S. Majety, V. A. Norman, L. Li, M. Bell, P. Saha, and M. Radulaski, "Quantum photonics in triangular-cross-section nanodevices in silicon carbide," *Journal of Physics: Photonics*, vol. 3, p. 34008, 2021.

[10] C. T. Nguyen, D. D. Sukachev, M. K. Bhaskar, B. Machielse, D. S. Levonian, E. N. Knall, P. Stroganov, R. Riedinger, H. Park, M. Lončar, and M. D. Lukin, "Quantum network nodes based on diamond qubits with an efficient nanophotonic interface," *Phys. Rev. Lett.*, vol. 123, p. 183602, 2019.

[11] J. L. Zhang, S. Sun, M. J. Burek, C. Dory, Y.-K. Tzeng, K. A. Fischer, Y. Kelaita, K. G. Lagoudakis, M. Radulaski, Z.-X. Shen, N. A. Melosh, S. Chu, M. Lončar, and J. Vučković, "Strongly cavity-enhanced spontaneous emission from silicon-vacancy centers in diamond," *Nano Letters*, vol. 18, no. 2, pp. 1360–1365, 2018. PMID: 29377701.

[12] M. J. Burek, C. Meuwly, R. E. Evans, M. K. Bhaskar, A. Sipahigil, S. Meesala, B. Machielse, D. D. Sukachev, C. T. Nguyen, J. L. Pacheco, E. Bielejec, M. D. Lukin, and M. Lončar, "Fiber-coupled diamond quantum nanophotonic interface," *Phys. Rev. Applied*, vol. 8, p. 024026, Aug 2017.

[13] R. Nagy, M. Widmann, M. Niethammer, D. B. R. Dasari, I. Gerhardt, Ö. O. Soykal, M. Radulaski, T. Ohshima, J. Vučković, N. T. Son, I. G. Ivanov, S. E. Economou, C. Bonato, S.-Y. Lee, and J. Wrachtrup, "Quantum properties of dichroic silicon vacancies in silicon carbide," *Physical Review Applied*, vol. 9, p. 034022, 2018.

[14] W. Li, L. Wang, L. Bian, F. Dong, M. Song, J. Shao, S. Jiang, and H. Guo, "Threshold displacement energies and displacement cascades in 4h-sic: Molecular dynamic simulations," *AIP Advances*, vol. 9, no. 5, p. 055007, 2019.

[15] F. Fuchs, B. Stender, M. Trupke, D. Simin, J. Pflaum, V. Dyakonov, and G. V. Astakhov, "Engineering near-infrared single-photon emitters with optically active spins in ultrapure silicon carbide," *Nature Communications*, vol. 6, no. 1, p. 7578, 2015.

[16] J. R. Weber, W. F. Koehl, J. B. Varley, A. Janotti, B. B. Buckley, C. G. Van de Walle, and D. D. Awschalom, "Quantum computing with defects," *Proceedings of the National Academy of Sciences*, vol. 107, pp. 8513–8518, 2010.

[17] D. McCloskey, D. Fox, N. O'Hara, V. Usov, D. Scanlan, N. McEvoy, G. S. Duesberg, G. L. W. Cross, H. Z. Zhang, and J. F. Donegan, "Helium ion microscope generated nitrogen-vacancy centres in type ib diamond," *Applied Physics Letters*, vol. 104, p. 031109, 2014.

[18] S. Castelletto and A. Boretti, "Silicon carbide color centers for quantum applications," *Journal of Physics: Photonics*, vol. 2, p. 022001, mar 2020.

[19] M. Widmann, M. Niethammer, T. Makino, T. Rendler, S. Lasse, T. Ohshima, J. Ul Hassan, N. Tien Son, S.-Y. Lee, and J. Wrachtrup, "Bright single photon sources in lateral silicon carbide light emitting diodes," *Applied Physics Letters*, vol. 112, no. 23, p. 231103, 2018.

[20] R. Nagy, D. B. R. Dasari, C. Babin, D. Liu, V. Vorobyov, M. Niethammer, M. Widmann, T. Linkewitz, I. Gediz, R. Stöhr, H. B. Weber, T. Ohshima, M. Ghezellou, N. T. Son, J. Ul-Hassan, F. Kaiser, and J. Wrachtrup, "Narrow inhomogeneous distribution of spin-active emitters in silicon carbide," *Applied Physics Letters*, vol. 118, p. 144003, 2021.

[21] S. Majety, V. A. Norman, L. Li, M. Bell, P. Saha, and M. Radulaski, "Quantum photonics in triangular-cross-section nanodevices in silicon carbide," *Journal of Physics: Photonics*, vol. 3, p. 34008, 2021.

[22] C. T. Nguyen, D. D. Sukachev, M. K. Bhaskar, B. Machielse, D. S. Levonian, E. N. Knall, P. Stroganov, R. Riedinger, H. Park, M. Lončar, and M. D. Lukin, "Quantum network nodes based on diamond qubits with an efficient nanophotonic interface," *Phys. Rev. Lett.*, vol. 123, p. 183602, 2019.

[23] J. L. Zhang, S. Sun, M. J. Burek, C. Dory, Y.-K. Tzeng, K. A. Fischer, Y. Kelaita, K. G. Lagoudakis, M. Radulaski, Z.-X. Shen, N. A. Melosh, S. Chu, M. Lončar, and J. Vučković, "Strongly cavity-enhanced spontaneous emission from silicon-vacancy centers in diamond," *Nano Letters*, vol. 18, no. 2, pp. 1360–1365, 2018. PMID: 29377701.

[24] M. J. Burek, C. Meuwly, R. E. Evans, M. K. Bhaskar, A. Sipahigil, S. Meesala, B. Machielse, D. D. Sukachev, C. T. Nguyen, J. L. Pacheco, E. Bielejec, M. D. Lukin, and M. Lončar, "Fiber-coupled diamond quantum nanophotonic interface," *Phys. Rev. Applied*, vol. 8, p. 024026, Aug 2017.